
Predicting quantum chemical property with easy-to-obtain geometry via positional denoising

Hyeonsu Kim^{1*} Jeheon Woo^{1*} Seonghwan Kim^{1*} Seokhyun Moon^{1*} Jun Hyeong Kim^{1*} Woo Youn Kim¹

Abstract

As quantum chemical properties have a significant dependence on their geometries, graph neural networks (GNNs) using 3D geometric information have achieved high prediction accuracy in many tasks. However, they often require 3D geometries obtained from high-level quantum mechanical calculations, which are practically infeasible, limiting their applicability in real-world problems. To tackle this, we propose a method to accurately predict the properties with relatively easy-to-obtain geometries (e.g., optimized geometries from the molecular force field). In this method, the input geometry, regarded as the corrupted geometry of the correct one, gradually approaches the correct one as it passes through the stacked denoising layers. We investigated the performance of the proposed method using 3D message-passing architectures for two prediction tasks: molecular properties and chemical reaction property. The reduction of positional errors through the denoising process contributed to performance improvement by increasing the mutual information between the correct and corrupted geometries. Moreover, our analysis of the correlation between denoising power and predictive accuracy demonstrates the effectiveness of the denoising process.

1. Introduction

Neural networks have been actively applied to various fields of molecular and quantum chemistry (Schütt et al., 2019; Manzhos & Carrington, 2020; Dral, 2020; Park et al., 2022). Several input representations, such as the SMILES string and graph-based representations, are employed to predict quantum chemical properties (David et al., 2020; Jiang et al., 2021). In particular, graph neural networks (GNNs), which operate on molecular graphs by updating the representation

of each atom via message-passing based on chemical bonds, have achieved great success in many molecular property prediction tasks (Schütt et al., 2018b; Yang et al., 2019; Xiong et al., 2019; Zhou et al., 2020; Moon et al., 2022; Kim et al., 2022).

However, as many quantum chemical properties significantly depend on molecular geometries, typical GNNs without 3D geometric information have limitations in their accuracy. In this respect, GNNs utilizing 3D information have recently achieved state-of-the-art accuracy (Schütt et al., 2018b; Gasteiger et al., 2020b; Liu et al., 2021b; Satorras et al., 2021). Despite of their impressive accuracy, the usage of the 3D input geometry is often infeasible in real-world applications, limiting the 3D GNNs' applicability (Lu et al., 2019; Stärk et al., 2021; Liu et al., 2021a; Xu et al., 2021; Chanussot et al., 2021). Therefore, it is natural to train machine learning models to make predictions with relatively easy-to-obtain geometries. For example, Lu et al. (2019) tried to predict a molecular property calculated by density functional theory (DFT) (Kohn & Sham, 1965) using geometries obtained with Merck Molecular Force Field (MMFF) (Halgren, 1996) optimization. They used transfer learning in which readout layers of the model trained on the QM9 dataset (Ramakrishnan et al., 2014) are fine-tuned on the QM9_M dataset (Lu et al., 2019), which predicts the same property with the MMFF geometry.

This study proposes a method for accurately predicting quantum chemical properties from relatively easy-to-obtain geometries through a denoising process. With the assumption that the easy-to-obtain geometry is a corrupted geometry that can be physically determined from the correct geometry, we devised a novel denoising process coupled with 3D message-passing neural networks. Hereafter, we denote the target property as Y and the correct and corrupted geometries as X and \tilde{X} , respectively. Various previous studies have been conducted on denoising approaches, such as a denoising autoencoder (DAE) (Vincent et al., 2008; 2010; Zhou et al., 2014; Godwin et al., 2021; Zaidi et al., 2022). The proposed method has the following differences from previous works: (1) While most denoising approaches have focused on improving prediction from X , the proposed method aims to improve the prediction accuracy from \tilde{X} .

*Equal contribution ¹Department of Chemistry, Korea Advanced Institute of Science and Technology, Daejeon, South Korea. Correspondence to: Woo Youn Kim <wooyoun@kaist.ac.kr>.

(2) In the denoising process, the input geometry is actually updated to approach X as it passes through the stacked DAE layers, which reduces accuracy degradation due to the use of corrupted geometries. (3) The training framework aims to capture the task-relevant information by jointly learning the auxiliary target, Y from X , along with the denoising. (4) Finally, our denoising process was designed to maximize mutual information (MI) among X , \tilde{X} , and Y .

We investigated the performance of the proposed method for two prediction tasks: (1) molecular properties of the QM9 and (2) a chemical reaction property. The QM9 dataset consists of molecular properties and corresponding geometries calculated by DFT. In this study, we focus on the problem of predicting the properties of the QM9 with MMFF geometries provided by the QM9_M dataset. Here, we consider the DFT and MMFF geometries as X and \tilde{X} , respectively. We also tested the proposed method to predict reaction barrier height for two datasets provided by Grambow et al. (2020b). The geometries of reactant and transition state (TS) molecules can be used to predict the barrier height because it is defined as the energy difference between the two geometries (Spiekermann et al., 2022b). However, we note that obtaining the TS geometry X^{TS} is computationally intractable (Pattanaik et al., 2020; Jackson et al., 2021; Spiekermann et al., 2022a), while the product molecule’s geometry X^P is relatively easy-to-obtain. In this task, the pair of geometries of reactant and TS molecules (X^R , X^{TS}) is considered as X , and the pair of geometries of reactant and product molecules (X^R , X^P) is considered as \tilde{X} .

We evaluated the performance of the proposed method through comparison with the baselines trained only with corrupted geometries using several 3D message-passing architectures. The performance of the previous state-of-the-art models (Lu et al., 2019; Spiekermann et al., 2022b) for the corresponding task were also compared, and the proposed method achieved the best prediction accuracy. The proposed method showed impressive performance, especially when the number of data was small in the QM9 task. Furthermore, the detailed analyses of the coefficient of the denoising loss support the effectiveness of the denoising process.

Our main contributions:

- To the best of our knowledge, we are the first to apply an explicit positional update in GNN layers for denoising.
- We presented the theoretical base of the positional denoising by relating with the MI and demonstrated its effectiveness by analyzing the correlation between geometries and properties.
- The proposed method was applied to practical tasks in chemistry, showing significant accuracy improvements

by denoising the easy-to-obtain geometry to the correct one.

- The proposed training framework is both simple and straightforward, which makes it highly adaptable for conventional 3D GNN architectures.

2. Related Work

2.1. Predicting high-level properties from easy-to-obtain geometry

Recently, several deep learning approaches have aimed to predict high-level properties from an easy-to-obtain geometry for accurate yet fast predictions in real-world applications. For instance, Molecule3D benchmark (Xu et al., 2021) aims to improve the applicability of existing 3D models by developing machine learning models that predict 3D geometry. These models predicted 3D geometry using 2D graph information that can be easily obtained and were evaluated using ETKDG (Riniker & Landrum, 2015) from RDKit (Contributors, 2021) as a baseline.

There have been attempts to predict high-level properties, starting with a geometry that can be quickly obtained by conventional methods, rather than machine learning methods. Lu et al. (2019) adopted MMFF geometries as the starting point, to predict high-level quantum mechanical properties of the molecules in the QM9 dataset. In chemical reactions, Spiekermann et al. (2022b) exploited reactant and product geometries to assess reaction barrier height rather than reactant and TS geometries; because obtaining the TS geometry is computationally challenging. Our study shares the same goal as these previous works.

2.2. Denoising approaches in GNN

Denoising is a commonly used approach for representation learning by recovering correct data from corrupted data. Previous studies have shown that models can learn desirable representations by mapping from a corrupted data manifold to a correct data manifold (Vincent et al., 2008; 2010). Recently, several studies in GNNs have adopted denoising strategies for representation learning and robustness during training (Hu et al., 2019; Sanchez-Gonzalez et al., 2020; Sato et al., 2021). For instance, Noisy Nodes (Godwin et al., 2021) used denoising as an auxiliary task to address oversmoothing in GNNs. Instead of using autoencoders for representation learning, they applied denoising to the noisy node information, resulting in improved performance in property prediction.

Furthermore, Xie et al. (2022) proposed a novel framework called LaGraph, which leverages predictive self-supervised learning of GNNs to predict the latent graph that represents semantic information of an observed graph. LaGraph in-

interprets the latent graph prediction as a generalized task of denoising approaches. In their interpretation, a corrupted graph of existing denoising methods is considered as the observed graph and a correct graph as the latent graph. To learn the mapping to the intractable latent graph using GNNs, they introduced a surrogate loss based on image representation learning (Xie et al., 2020), demonstrating the effectiveness of their proposed approach related to other representation learning methods.

In our approach, we consider easy-to-obtain geometries lying on a geometrically corrupted data manifold and aim to maximize the MI between the message from the corrupted data and correct data through a denoising process. Unlike existing denoising techniques like Noisy Nodes that learn by denoising noise sampled from a zero-mean distribution, our experiments use physically determined correct data X and corrupted data \tilde{X} . This means that the noise distribution we use is different from a zero-mean distribution. Finally, our approach differs from previous methods in that it predicts the attributes of correct data from easy-to-obtain data that conventional techniques consider corrupted. This strategy is particularly significant in chemistry, where obtaining high-level computational data is expensive.

2.3. Equivariant 3D GNNs for quantum chemical properties

In the field of chemistry, GNNs utilizing 3D geometric information have shown promising performance in predicting quantum chemical or systematic properties (Schütt et al., 2018b;a; Gasteiger et al., 2020b;a; 2021; Liu et al., 2021b; Satorras et al., 2021; Wang et al., 2022). Since target physical quantities, such as an energy, are invariant to alignments of a molecule, 3D GNN models utilize roto-translational invariant 3D information as their inputs (Schütt et al., 2021; Jing et al., 2020). As a representative example, a distance matrix guarantees the invariance because the roto-translational transformation does not vary distances. SchNet (Schütt et al., 2018b;a) and EGNN (Satorras et al., 2021) are proper examples of utilizing the distance matrix. The former exploits the radial basis function based on the distance matrix, while the latter uses distance information directly on the GNN message-passing scheme. In DimeNet++ (Gasteiger et al., 2020a), along with the distance matrix, bond angles are also available as invariant 3D information. In addition, ComENet (Wang et al., 2022) and SphereNet (Liu et al., 2021b) introduced dihedral angles in addition to the distance and bond angle information. Likewise, our method ensures the equivariance because it directly updates the position vector of models utilizing the distance matrix.

3. Method

3.1. Problem setting

Our primary goal is learning the mapping from the easy-to-obtain geometry, \tilde{X} , to the quantum chemical property, Y , of the correct geometry, X . Unlike general supervision tasks, our training data, \mathcal{D} , consist of observed samples (x, \tilde{x}, y) from triplet of three random variables X , \tilde{X} , and Y . We assume the data are i.i.d. sampled from unknown distribution $q(X, \tilde{X}, Y)$.

Under our problem setting, y can be directly attained from the x . In contrast, geometry transformation from \tilde{x} to x should be preceded to get y from \tilde{x} . Thus, we can assume the following:

Assumption 3.1. \tilde{X} and Y are conditionally independent given X as $q(Y|X, \tilde{X}) = q(Y|X)$.

Since physical correlation between X and Y is higher than that between \tilde{X} and Y , learning the transformation from \tilde{X} to X could improve prediction performance. In this work, we introduced this transformation in the form of positional update similar to denoising process of DAE. Meanwhile, in order to leverage information between X and Y , we added an auxiliary loss for the prediction of Y from X . We emphasize that the proposed method utilizes two auxiliary losses in addition to the primary training target, which is equivalent to maximizing the MI of X , \tilde{X} , and Y .

3.2. Training objectives

Mutual information. The MI, $I(X; \tilde{X}; Y)$, measures the non-linear dependence among three random variables X , \tilde{X} , and Y (Belghazi et al., 2018). Therefore, a more robust mapping from \tilde{X} to Y can be obtained by maximizing this correlation. In addition, we confirm that Assumption 3.1 leads to Proposition 3.2.

Proposition 3.2. For any triplets of random variables (X, \tilde{X}, Y) , if \tilde{X} and Y are conditionally independent given X , then $-H(Y|\tilde{X}) = I(X; \tilde{X}; Y)$.

By Proposition 3.2, $I(X; \tilde{X}; Y)$ can be considered as an unbiased training target for the primary goal of predicting Y from \tilde{X} . However, because $I(X; \tilde{X}; Y)$ is intractable, instead of directly maximizing it, we set a tractable lower bound (Proposition 3.3) and maximize it.

Proposition 3.3. $I(X; \tilde{X}; Y) \geq LB + 2H(Y) \forall r.v. X, \tilde{X}, Y$, where $LB = -2H(Y|X) - H(Y|\tilde{X}) - H(X|\tilde{X})$.

According to the propositions, we have three optimization targets as follows: (1) property prediction from corrupted geometry, (2) property prediction from correct geometry,

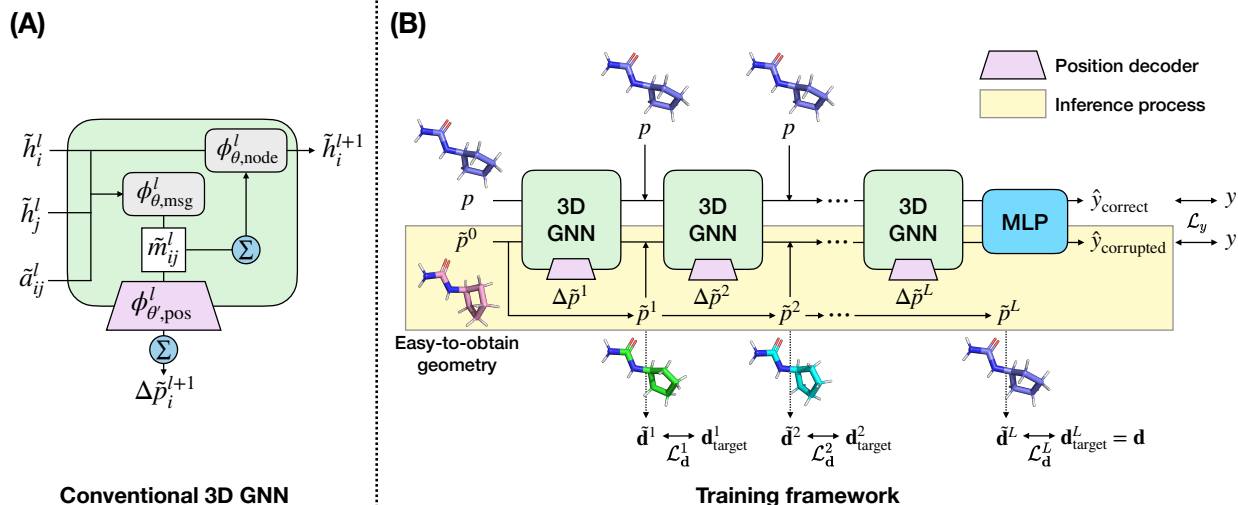


Figure 1: (A) Message propagation scheme of the conventional 3D GNN with a positional update. (B) Schematic illustration of the proposed training framework.

and (3) denoising target.

$$H(Y|\tilde{X}) = \mathbb{E}_{q(\tilde{X}, Y)} [-\log q(Y|\tilde{X})] \quad (1)$$

$$H(Y|X) = \mathbb{E}_{q(X, Y)} [-\log q(Y|X)] \quad (2)$$

$$H(X|\tilde{X}) = \mathbb{E}_{q(X, \tilde{X})} [-\log q(X|\tilde{X})] \quad (3)$$

3.3. Training framework

Overall training scheme. We first briefly describe the general model architecture and terminology of GNN using 3D geometry. 3D GNNs utilize geometric graph $\mathcal{G} = (\mathcal{V}, \mathcal{E}, \mathcal{P})$ as input. The graph comprises the nodes $v_i \in \mathcal{V}$, edges $e_{ij} \in \mathcal{E}$, and positions $p_i \in \mathcal{P}$, where i and j are distinct node indices. In a molecular graph, nodes and edges refer to atoms and connection information, respectively, and positions refer to atomic positions. Each layer of 3D GNN consists of message generation, message gathering, and node update step:

$$m_{ij} = \phi_{\text{msg}}(h_i^l, h_j^l, a_{ij}^l; \theta), \quad (4)$$

$$m_i = \sum_{j \in \mathcal{N}(i)} m_{ij}, \quad (5)$$

$$h_i^{l+1} = \phi_{\text{node}}(h_i^l, m_i; \theta), \quad (6)$$

where $h_i^l \in \mathbb{R}^d$ denotes the d -dimensional hidden vector of node v_i at l^{th} layer, and a_{ij} denotes the edge information containing distance information between i^{th} and j^{th} nodes. $\mathcal{N}(i)$ represents a set of all node indices connected to node

v_i . In addition, there is a positional update step in each layer of EGNN (Satorras et al., 2021) along with the node representation update as follows:

$$p_i^{l+1} = p_i^l + \sum_{j \in \mathcal{N}(i)} (p_i^l - p_j^l) \phi_{\text{pos}}(m_{ij}; \theta'), \quad (7)$$

where p_i^l indicates i^{th} atomic position at l^{th} layer. Overall 3D GNN propagation process with positional update is presented in Figure 1(A). Since DimeNet++ (Gasteiger et al., 2020a) utilizes additional angle information, we provide a detailed description of the message-passing and positional update scheme for it in Appendix E.

Figure 1(B) shows the overall training framework, given a sampled data (x, \tilde{x}, y) . The proposed method regards the message generation as an encoder, $\phi_{\theta, \text{msg}}$, parameterized by θ and the positional update of EGNN as a position decoder, $\phi_{\theta', \text{pos}}$, parameterized by θ' . Our approach utilizes \tilde{x} for predicting y in both the training and testing phases. To mitigate positional noise in \tilde{x} , we adopt a stacked encoder-decoder architecture that performs positional denoising in a stepwise manner. In the training process, one can maximize MI by additionally predicting y from x along with the denoising process, sharing the weights of the encoder. This encoder-decoder framework with MI training target can be applied to conventional 3D GNN models. During the inference process, highlighted in yellow in Figure 1(B), the model takes only an easy-to-obtain geometry \tilde{x} as input. It goes through layers with trained encoder-decoders and is gradually denoised. In the final layer, the multi-layer perceptron (MLP) predicts the property based on the denoised geometry.

Relevance to denoising autoencoder The proposed posi-

tional update process shares the background with DAE. Conventional DAEs run simple process of mapping a corrupted sample to a correct sample. Informally speaking, DAE aims to obtain a good representation M describing X , which is achieved through maximizing $I(M; X)$. The training target of DAE is to maximize $\mathbb{E}_{q(X, M)}[\log p(X|M)]$, which is equivalent to maximizing $I(\tilde{X}; X)$ when the encoder is a deterministic injective function (Proposition B.1). In general DAE, the injective assumption is infeasible because multiple corrupted samples correspond to the correct one. On the other hand, in our problem setting, the injective assumption is natural because \tilde{x} is physically unique given x . Our method describes the process of gradually optimizing a corrupted geometry into a correct one through stacked DAE layers. From a positional point of view, this can be interpreted as a denoising process.

SE(3) invariant denoising loss. The geometries of x and \tilde{x} both belong to Euclidean space $\mathbb{R}^{N \times 3}$. On the other hand, we are not assuming that the geometries of X and \tilde{X} are aligned with each other. That is, for any data sample (x, \tilde{x}, y) and for any SE(3) transformation g , the sampling probability of $(g \cdot x, \tilde{x}, y)$ should be equal to that of (x, \tilde{x}, y) . Accordingly, the conditional probability of x given \tilde{x} satisfies the following:

$$q(X = x | \tilde{X} = \tilde{x}) = q(X = g \cdot x | \tilde{X} = \tilde{x}). \quad (8)$$

We note that this conditional probability is an unbiased training target distribution of the denoising process. Since we want the denoising process to be deterministic, we define a probability at distance matrix domain that are invariant to the transformations. Let a mapping D from position space to distance space be as following, $D : p \in \mathbb{R}^{N \times 3} \rightarrow \mathbf{d} \in \mathbb{R}^{N \times N}$ such that $D(p)_{ij} = \|p_i - p_j\|_2$. Set of all points that can be reached by any SE(3) transformation, $\{(g_1 \cdot x, g_2 \cdot \tilde{x}) | \forall g_1, g_2 \in \text{SE}(3)\}$, is collapsed to a single point when mapped to distance matrix domain. We assume that the distributions in distance space and in Euclidean space would be expressed locally as the same family. Therefore, we make the denoising loss tractable by replacing $q(X|\tilde{X})$ with $q(\mathbf{d}|\tilde{\mathbf{d}})$ through this mapping. A model prediction probability, $p(X|\tilde{X}; \theta)$, also can be replaced as $p(\mathbf{d}|\tilde{\mathbf{d}}; \theta)$.

Loss functions. The overall loss function is derived from three training targets of Proposition 3.3 (see Appendix B).

$$\mathcal{L} = \mathcal{L}_{y, \text{corrupted}} + \mathcal{L}_{y, \text{correct}} + \lambda \sum_l \mathcal{L}_d^l \quad (9)$$

$$\mathcal{L}_{y, \text{corrupted}} = \frac{1}{n} \sum_{i=1}^n |y_i - \hat{y}_{i, \text{corrupted}}| \quad (10)$$

$$\mathcal{L}_{y, \text{correct}} = \frac{1}{n} \sum_{i=1}^n |y_i - \hat{y}_{i, \text{correct}}| \quad (11)$$

$$\mathcal{L}_d^l = \frac{1}{n} \sum_{i=1}^n \|\mathbf{d}_{i, \text{target}}^l - \tilde{\mathbf{d}}_i^l\|_1 \quad (12)$$

Here, n is the number of training samples. Property prediction losses are mean absolute errors (MAEs) of predicted outputs $\hat{y}_{\text{corrupted}}$ and \hat{y}_{correct} , which are from the input of corrupted geometry \tilde{x} and correct geometry x , respectively (Equations (10) and (11)). The l^{th} positional denoising loss is an averaged absolute difference between the l^{th} target distance matrix $\mathbf{d}_{\text{target}}^l$ and the denoised distance matrix $\tilde{\mathbf{d}}^l$ of the l^{th} layer’s output geometry \tilde{p}^l (Equation (12)).

In consideration of practical constraints, such as the limited expressive power of a single DAE layer, it appeared challenging to directly map \tilde{x} to x for first few layers. To tackle this, we have chosen to set the gradual denoising loss of which $\mathbf{d}_{\text{target}}^l$ is gradually adjusted to approach x starting from \tilde{x} , despite the presence of discrepancy with theoretically derived target $\mathbf{d}_{\text{target}}^l = \mathbf{d}$ (see Appendix A.2). In the total loss function, λ is a hyperparameter for adjusting the weight of distance matrix MAE losses.

3.4. Theoretical insight

The goal of maximizing MI is to extract as much relevant information about the target property Y as possible from the corrupted geometry \tilde{X} . Let (x, \tilde{x}, y) be an observed sample. Given that y is observed from the correct geometry x , we can assume that representations from x contain higher quality information than those from \tilde{x} . Building on this assumption, we trained two auxiliary targets alongside the primary target, leveraging x to obtain a more informative representation. Through the process of mapping the representation of \tilde{x} to x , we induce it to capture physically meaningful information about x . By mapping the representation of x to y , the shared encoder can capture unbiased and fruitful information about y , free from any distortions or biases introduced by \tilde{x} . Our method can be likened to self-supervised learning, as both focus on the learning high-quality representations. However, our approach is distinguished by its emphasis on a specialized representation that is tailored to the specific property. By prioritizing the acquisition of task-relevant information, rather than solely focusing on the property, we can expect to achieve more robust predictions.

4. Results and Discussion

4.1. Molecular property prediction

Predicting molecular properties is crucial to various fields in chemistry. The QM9 is the widely used benchmark dataset for molecular property prediction comprised of 134k molecule information; each molecule consists of at most nine heavy atoms (C, N, O, and F). Each data sample con-

Table 1: MAEs for QM9_M's properties. Our method was tested with three different 3D GNNs. Both Transformer-M's predictions were made with 2D molecular graphs as input.

| TARGET | UNIT | EGNN | | SCHNET | | DIME NET++ | | TRANSFORMER-M | |
|--------------------------|--|--------|--------|--------|--------|------------|-------|---------------|--------|
| | | BASE | OURS | BASE | OURS | BASE | OURS | 2D | 2D+3D |
| U_0 | meV | 17.4 | 14.5 | 27.3 | 27.3 | 16.9 | 14.0 | 38.2 | 43.9 |
| μ | D | 0.133 | 0.0996 | 0.208 | 0.139 | 0.139 | 0.127 | 0.309 | 0.245 |
| α | Bohr ³ | 0.125 | 0.105 | 0.160 | 0.131 | 0.123 | 0.109 | 0.171 | 0.160 |
| ϵ_{HOMO} | meV | 38.4 | 35.7 | 61.4 | 52.0 | 37.5 | 35.0 | 53.6 | 48.7 |
| ϵ_{LUMO} | meV | 34.4 | 31.2 | 53.9 | 45.0 | 35.1 | 32.6 | 52.5 | 46.3 |
| GAP | meV | 58.0 | 53.2 | 85.8 | 74.4 | 56.3 | 55.3 | 77.1 | 68.4 |
| R^2 | Bohr ² | 5.60 | 4.08 | 8.32 | 6.44 | 5.82 | 5.29 | 11.4 | 10.3 |
| C_v | $\frac{\text{cal}}{\text{mol}\cdot\text{K}}$ | 0.0445 | 0.0407 | 0.0595 | 0.0566 | 0.0462 | 0.418 | 0.0669 | 0.0683 |
| ZPVE | meV | 1.97 | 1.76 | 2.57 | 2.38 | 2.10 | 1.90 | 4.79 | 3.85 |

tains optimized geometry and corresponding quantum mechanical properties obtained by DFT calculations.

This study focuses on the QM9_M task which predicts DFT properties using the MMFF geometry. The QM9_M dataset originated from the QM9 data differs only in the molecular geometry; each geometry herein has been obtained with additional MMFF optimization starting with the corresponding geometry in the QM9. Here, the MMFF geometry is regarded as a relatively easy-to-obtain geometry compared to the DFT geometry.

Training setup. This study employed the following three GNNs using distinct invariant 3D information to demonstrate the effectiveness of our method: EGNN (Atz et al., 2022), SchNet (Schütt et al., 2018a), and DimeNet++ (Gasteiger et al., 2020a). We appended the positional update to the SchNet and DimeNet++ to ensure that the denoising process can be applied to them in the same manner in the coordinate update of the EGNN. To train the models, we considered the DFT geometry from the QM9 dataset, namely X , and the corresponding MMFF geometry from QM9_M dataset, namely \tilde{X} . Molecular 2D graphs are similar to MMFF geometries in that they are easy-to-obtain information than DFT geometries. Luo et al. (2022) demonstrated that the prediction accuracy based on molecular 2D graphs can be improved by using not only molecular 2D graphs but also DFT geometries and 3D positional denoising during the training step. Therefore, for comparison, we confirmed the prediction performance of Transformer-M whether the use of DFT geometries in the training step. We used 100,000, 18,000, and 13,000 molecules for training, validation, and testing, respectively, as in previous work by Satorras et al. (2021). The detailed hyperparameters of each model are introduced in Appendix D.1. Hereafter, for all target properties, we denote the trained models using our method as "OURS" and the trained models using only \tilde{X} and X as the baseline ("BASE") and ground truth ("GT"), respectively.

Results on molecular property prediction. Table 1 demonstrates that our method leads to performance improvements across all properties and models. In detail, our method resulted in accuracy improvements of 7.0~27% for EGNN, 0.0~33% for SchNet, and 6.4~14% for DimeNet++, compared to their respective baselines. The Transformer-M using molecular 2D graphs resulted in accuracy improvements of -15~21% compared to the model trained using only 2D graphs. It is noteworthy that for most properties, Transformer-M was less accurate than the investigated baseline 3D models. This result implies that both the MMFF geometry and the molecular 2D graph are easy-to-obtain input than the DFT geometry, but the MMFF geometry involves more useful information than the 2D graph to learn the relationship between molecules and their quantum chemical properties. Hereafter, we conducted subsequent analyses using EGNN because it showed the best performance in the QM9_M task.

Prediction performance according to training set sizes.

Table 2 shows the predictive performance of the baselines, trained models using our method, and the ground truth according to the training set sizes for the prediction of U_0 property. It also contains DTNN results (DTNN_{TL} and DTNN_{GT}) of Lu et al. (2019). In detail, DTNN_{TL}

 Table 2: MAEs (meV) on prediction of U_0 with different training set sizes and input geometries.

| | INPUT | 10K | 25K | 50K | 100K |
|----------------------|-------------|------|------|------|------|
| EGNN _{BASE} | \tilde{X} | 70.0 | 38.0 | 25.8 | 17.4 |
| EGNN _{OURS} | \tilde{X} | 56.3 | 31.6 | 20.0 | 14.5 |
| EGNN _{GT} | X | 59.6 | 31.7 | 21.7 | 12.9 |
| DTNN _{TL} | \tilde{X} | - | 64.6 | 43.8 | 34.3 |
| DTNN _{GT} | X | - | 29.9 | 20.0 | 14.7 |
| EGNN _{OURS} | X | 54.5 | 30.0 | 18.5 | 12.4 |

Table 3: The Pearson correlation coefficients between D-MAE and P-MAE (ρ_{DP}) for R^2 , μ , and U_0 in the QM9_M. The coefficient values were compared for the baseline and the model using our method.

| PROPERTY | EGNN _{BASE} | EGNN _{OURS} |
|----------|----------------------|----------------------|
| R^2 | 0.445 | 0.667 |
| μ | 0.363 | 0.494 |
| U_0 | 0.094 | 0.264 |

was trained with transfer learning, and the model also focused on predicting the quantum chemical property using \tilde{X} . The improvement tendency of DTNN_{GT} performance according to the number of data was similar to that of EGNN_{GT}. However, EGNN_{OURS} using \tilde{X} as input showed some differences compared to DTNN_{TL}. Impressively, the EGNN_{OURS} outperformed EGNN_{GT} when the number of data is lower than 50K. In this regard, we expected our method can be utilized in various chemistry fields with a lack of data. We also confirmed that EGNN_{OURS} using X as input outperforms EGNN_{GT}. These results can be understood as the effect of maximization of the MI of X , \tilde{X} , and Y .

Understanding different denoising effects depending on properties. As shown in Table 7, the prediction accuracy was improved for all properties as the input gets closer to the X , implying that \tilde{X} is the corrupted version of X . Therefore, our method, which utilizes a denoising process, can predict molecular properties accurately despite using \tilde{X} . The larger the accuracy degradations of the baseline compared to the ground truth, the more significant improvements in accuracy achieved through our method for EGNN (see Tables 1 and 7). For further understanding, we focused on the accuracy degradation by varying the degree of corruption of the input geometry. We selected μ and R^2 , showing large accuracy degradations, and U_0 , showing a relatively small accuracy degradation. We calculated the MAE of property prediction (P-MAE) for each property and distance matrix MAE (D-MAE) between X and \tilde{X} . Then, we calculated the Pearson correlation coefficients between D-MAE and P-MAE (ρ_{DP}) for μ , R^2 , and U_0 , respectively (see Table 3). In baseline models, ρ_{DP} of U_0 was very low at 0.094, while ρ_{DP} of μ and R^2 were high at 0.363 and 0.494, respectively. It means that D-MAE and P-MAE have a relatively larger positive correlation in μ and R^2 than in U_0 . Thus, it can be interpreted that the prediction accuracy of μ and R^2 is sensitive to the input geometry. When our method was applied, we calculated D-MAE between X and positional updated \tilde{X} at the last GNN layer. ρ_{DP} of μ , R^2 , and U_0 increased to 0.494, 0.667, and 0.264, respectively. We also confirmed that the coefficient of each property increased with the introduction of our method for molecules

Table 4: MAEs for μ , R^2 , and U_0 with different λ values on EGNN.

| λ | R^2 (Bohr ²) | μ (D) | U_0 (meV) |
|-----------|----------------------------|---------------|-------------|
| 0.1 | 4.96 | 0.125 | 14.5 |
| 0.5 | 4.24 | 0.109 | 16.8 |
| 1.0 | 4.08 | 0.0996 | 17.0 |
| 10.0 | 4.52 | 0.105 | 20.7 |

in the out-of-distributions (see Appendix A.4). Thus, on average, the more accurate prediction was possible as \tilde{X} approaches X , supporting that our proposed ‘‘denoising from the perspective of geometry’’ worked effectively.

Additionally, we analyzed the effect of the coefficient λ in the loss function (Equation (9)), which represents the importance of the denoising process in the training phase. Table 4 shows that optimal λ values of μ and R^2 are higher than that of U_0 . It is consistent with our intuition that the optimal λ values for μ and R^2 expected to be high due to being tightly correlated with the input geometry compared to other properties.

4.2. Reaction property prediction

A chemical reaction is a process in which reactant molecules convert to product molecules, passing through their TS. Predicting properties related to the reaction is important for understanding the nature of the chemistry (Grambow et al., 2020a). The barrier height as one of the reaction properties is defined as the energy difference between X^{TS} and X^R . Commonly, optimizing a X^{TS} utilizes both X^R and X^P . However, this optimization process is typically resource-intensive, requiring approximately 10 times more computational resources compared to optimizing X^R or X^P individually (Palazzesi et al., 2020). Thus, predicting accurate barrier height without X^{TS} is necessary to reduce computational costs.

From this point of view, we focused on the task to predict DFT calculation-based barrier heights using (X^R , X^P) for the elementary reaction of the gas phase, as reported by Spiekermann et al. (2022b). In contrast to most molecular

Table 5: MAEs for predicted reaction barrier (kcal/mol) using \tilde{X} as input. D-MPNN, BASELINE, and OURS indicate the 2D D-MPNN model, 3D DimeReaction, and 3D DimeReaction using our method, respectively.

| DATASET | D-MPNN | BASELINE | OURS |
|-------------|--------|----------|------|
| CCSD(T)-UNI | 4.59 | 6.03 | 3.90 |
| B97-D3 | 4.91 | 7.32 | 4.17 |

Table 6: Ablation study for our method. BH indicates the reaction barrier height. The performance was evaluated in terms of MAE.

| DATASET | PROPERTY | UNIT | OURS | w/o \mathcal{L}_d^l | w/o POSITIONAL UPDATE | w/o $\mathcal{L}_{y,\text{correct}}$ |
|----------------------|----------|-------------------|--------|-----------------------|-----------------------|--------------------------------------|
| QM9+QM9 _M | U_0 | meV | 14.5 | 21.0 | 14.2 | 15.2 |
| | R^2 | Bohr ² | 4.08 | 6.43 | 4.12 | 4.43 |
| | C_v | cal/mol · K | 0.0407 | 0.0503 | 0.0410 | 0.0401 |
| | μ | D | 0.0997 | 0.127 | 0.111 | 0.110 |
| CCSD(T)-UNI | BH | kcal/mol | 3.90 | 4.41 | 5.77 | 4.27 |
| B97-D3 | BH | kcal/mol | 4.17 | 4.49 | 7.19 | 4.45 |

properties, the property is a function of not just a single molecular geometry, but $(X^R, X^T S)$, which can be interpreted as an optimized version of (X^R, X^P) . Thus, we considered that $X := (X^R, X^T S)$ and $\tilde{X} := (X^R, X^P)$ in this task.

We used two datasets (Spiekermann et al., 2022b) for comparison with the previous work. The first dataset consists of unimolecular reactions, namely CCSD(T)-UNI. The second dataset, B97-D3, has 16,365 reactions.

Training setup. Spiekermann et al. (2022a) proposed two models for predicting the barrier height using the 2D and 3D information of \tilde{X} , respectively. They used D-MPNN for 2D GNN and DimeNet++ for 3D GNN, which will be referred to as the 2D D-MPNN model and the 3D DimeReaction, respectively. They reported the 3D DimeReaction model trained using \tilde{X} showed lower performance than that of 2D D-MPNN model because accuracy of the 3D model was sensitive to the noise in the input geometry. Thus, our method, which removes the noise, can be useful for 3D DimeReaction.

For the 3D DimeReaction, we employed different positional update strategy from the molecular property prediction by updating only the position of X^P using both X^R and X^P . We trained the 2D D-MPNN model, 3D DimeReaction, and 3D DimeReaction using our method for CCSD(T)-UNI and B97-D3 datasets. The used data split and augmentation were the same as in the previous work by Spiekermann et al. (2022a). The hyperparameters used are described in Appendix D.1.

Results on reaction property prediction. We denote the 3D DimeReaction model trained using only \tilde{X} as a baseline. To evaluate the performance of our method, we trained 2D D-MPNN model, baseline, and 3D DimeReaction model using our method. The results are shown in Table 5. Our method showed performance improvements compared to the baseline as it resulted in accuracy improvements of 35.4% and 43.0% in terms of MAE for the CCSD(T)-UNI and B97-D3 datasets, respectively. It also outperformed the 2D D-MPNN model, the state-of-the-art model in this task.

4.3. Ablation study

Our method uses a combination of denoising loss, $\mathcal{L}_{y,\text{correct}}$, and the positional update to improve the accuracy of predicting quantum chemical properties using \tilde{X} . To verify the individual contributions of each strategy of our method, we conducted ablation studies. Table 6 shows that all strategies are individually meaningful to reduce prediction error regardless of the properties. As a result, the combination of all three strategies yielded the best accuracy.

In the molecular property prediction task, we observed performance improvements in the following order: denoising loss term, $\mathcal{L}_{y,\text{correct}}$, and positional update. However, in the case of the reaction property prediction task, the positional update method showed the highest performance, followed by denoising loss and $\mathcal{L}_{y,\text{correct}}$. In general, we found that incorporating denoising loss significantly improved performance on both datasets and that positional update had a particularly strong impact on the reaction dataset. This might be attributed to the significant geometric differences between \tilde{X} and X in terms of D-MAE. The positional update method can lead to more accurate predictions for the situation due to capturing effectively the information of X .

5. Conclusion

The proposed training framework involving the denoising process enables accurate prediction using the easy-to-obtain geometry, regarded as the corrupted version of the correct geometry. With the theoretical basis that the denoising process maximizes the mutual information between correct and corrupted geometries, the proposed method reduced the accuracy degradation due to the use of corrupted geometries. In particular, the positional update in the denoising process is the unique feature of the proposed method. An analysis of the correlation between the denoising effect and predictive accuracy in the QM9_M task demonstrated the effectiveness of the denoising process.

The proposed method showed remarkable improvements when the number of data was small in the QM9_M task. In this respect, we expect that the proposed method will be

useful for many other tasks that suffer from a lack of data.

We also note that the presented models can be improved by the hyperparameters search, as we utilized the same size of the model used in previous work to confirm only the impact of our method compared to the results of the previous works. Our codes will be available as soon as possible.

References

- Atz, K., Isert, C., Böcker, M. N. A., Jiménez-Luna, J., and Schneider, G. Δ -quantum machine-learning for medicinal chemistry. *Physical Chemistry Chemical Physics*, 24(18):10775–10783, 2022. doi: 10.1039/d2cp00834c. URL <https://doi.org/10.1039/d2cp00834c>.
- Belghazi, M. I., Baratin, A., Rajeshwar, S., Ozair, S., Bengio, Y., Courville, A., and Hjelm, D. Mutual information neural estimation. In Dy, J. and Krause, A. (eds.), *Proceedings of the 35th International Conference on Machine Learning*, volume 80 of *Proceedings of Machine Learning Research*, pp. 531–540. PMLR, 10–15 Jul 2018. URL <https://proceedings.mlr.press/v80/belghazi18a.html>.
- Bemis, G. W. and Murcko, M. A. The properties of known drugs. 1. molecular frameworks. *Journal of Medicinal Chemistry*, 39(15):2887–2893, January 1996. doi: 10.1021/jm9602928. URL <https://doi.org/10.1021/jm9602928>.
- Chanussot, L., Das, A., Goyal, S., Lavril, T., Shuaibi, M., Riviere, M., Tran, K., Heras-Domingo, J., Ho, C., Hu, W., Palizhati, A., Sriram, A., Wood, B., Yoon, J., Parikh, D., Zitnick, C. L., and Ulissi, Z. Open catalyst 2020 (OC20) dataset and community challenges. *ACS Catalysis*, 11(10):6059–6072, May 2021. doi: 10.1021/acscatal.0c04525. URL <https://doi.org/10.1021/acscatal.0c04525>.
- Contributors, R. Rdkit: Open-source cheminformatics, 2021. URL <http://www.rdkit.org/>. Accessed: 2023-03-19.
- David, L., Thakkar, A., Mercado, R., and Engkvist, O. Molecular representations in AI-driven drug discovery: a review and practical guide. *Journal of Cheminformatics*, 12(1), September 2020. doi: 10.1186/s13321-020-00460-5. URL <https://doi.org/10.1186/s13321-020-00460-5>.
- Dral, P. O. Quantum chemistry in the age of machine learning. *The Journal of Physical Chemistry Letters*, 11(6):2336–2347, March 2020. doi: 10.1021/acs.jpclett.9b03664. URL <https://doi.org/10.1021/acs.jpclett.9b03664>.
- Gasteiger, J., Giri, S., Margraf, J. T., and Günnemann, S. Fast and uncertainty-aware directional message passing for non-equilibrium molecules, 2020a. URL <https://arxiv.org/abs/2011.14115>.
- Gasteiger, J., Groß, J., and Günnemann, S. Directional message passing for molecular graphs, 2020b. URL <https://arxiv.org/abs/2003.03123>.
- Gasteiger, J., Becker, F., and Günnemann, S. Gemnet: Universal directional graph neural networks for molecules. *Advances in Neural Information Processing Systems*, 34: 6790–6802, 2021.
- Godwin, J., Schaarschmidt, M., Gaunt, A., Sanchez-Gonzalez, A., Rubanova, Y., Veličković, P., Kirkpatrick, J., and Battaglia, P. Simple gnn regularisation for 3d molecular property prediction & beyond, 2021. URL <https://arxiv.org/abs/2106.07971>.
- Grambow, C. A., Pattanaik, L., and Green, W. H. Deep learning of activation energies. *The Journal of Physical Chemistry Letters*, 11(8):2992–2997, March 2020a. doi: 10.1021/acs.jpclett.0c00500. URL <https://doi.org/10.1021/acs.jpclett.0c00500>.
- Grambow, C. A., Pattanaik, L., and Green, W. H. Reactants, products, and transition states of elementary chemical reactions based on quantum chemistry. *Scientific Data*, 7(1), May 2020b. doi: 10.1038/s41597-020-0460-4. URL <https://doi.org/10.1038/s41597-020-0460-4>.
- Halgren, T. A. Merck molecular force field. i. basis, form, scope, parameterization, and performance of MMFF94. *Journal of Computational Chemistry*, 17(5-6):490–519, April 1996. doi: 10.1002/(sici)1096-987x(199604)17:5/6<490::aid-jcc1>3.0.co;2-p. URL [https://doi.org/10.1002/\(sici\)1096-987x\(199604\)17:5/6<490::aid-jcc1>3.0.co;2-p](https://doi.org/10.1002/(sici)1096-987x(199604)17:5/6<490::aid-jcc1>3.0.co;2-p).
- Hu, W., Liu, B., Gomes, J., Zitnik, M., Liang, P., Pande, V., and Leskovec, J. Strategies for pre-training graph neural networks. *arXiv preprint arXiv:1905.12265*, 2019.
- Jackson, R., Zhang, W., and Pearson, J. TSNet: predicting transition state structures with tensor field networks and transfer learning. *Chemical Science*, 12(29): 10022–10040, 2021. doi: 10.1039/d1sc01206a. URL <https://doi.org/10.1039/d1sc01206a>.
- Jiang, D., Wu, Z., Hsieh, C.-Y., Chen, G., Liao, B., Wang, Z., Shen, C., Cao, D., Wu, J., and Hou, T. Could graph neural networks learn better molecular representation for drug discovery? a comparison study of descriptor-based and graph-based models. *Journal of Cheminformatics*, 13(1), February 2021. doi:

- 10.1186/s13321-020-00479-8. URL <https://doi.org/10.1186/s13321-020-00479-8>.
- Jing, B., Eismann, S., Suriana, P., Townshend, R. J., and Dror, R. Learning from protein structure with geometric vector perceptrons. *arXiv preprint arXiv:2009.01411*, 2020.
- Kim, J. H., Kim, H., and Kim, W. Y. Effect of molecular representation on deep learning performance for prediction of molecular electronic properties. *Bulletin of the Korean Chemical Society*, 43(5):645–649, March 2022. doi: 10.1002/bkcs.12516. URL <https://doi.org/10.1002/bkcs.12516>.
- Kohn, W. and Sham, L. J. Self-consistent equations including exchange and correlation effects. *Phys. Rev.*, 140: A1133–A1138, Nov 1965. doi: 10.1103/PhysRev.140.A1133. URL <https://link.aps.org/doi/10.1103/PhysRev.140.A1133>.
- Liu, S., Wang, H., Liu, W., Lasenby, J., Guo, H., and Tang, J. Pre-training molecular graph representation with 3d geometry, 2021a. URL <https://arxiv.org/abs/2110.07728>.
- Liu, Y., Wang, L., Liu, M., Zhang, X., Oztekin, B., and Ji, S. Spherical message passing for 3d graph networks, 2021b. URL <https://arxiv.org/abs/2102.05013>.
- Lu, J., Wang, C., and Zhang, Y. Predicting molecular energy using force-field optimized geometries and atomic vector representations learned from an improved deep tensor neural network. *Journal of Chemical Theory and Computation*, 15(7):4113–4121, May 2019. doi: 10.1021/acs.jctc.9b00001. URL <https://doi.org/10.1021/acs.jctc.9b00001>.
- Luo, S., Chen, T., Xu, Y., Zheng, S., Liu, T.-Y., Wang, L., and He, D. One transformer can understand both 2d & 3d molecular data, 2022.
- Manzhos, S. and Carrington, T. Neural network potential energy surfaces for small molecules and reactions. *Chemical Reviews*, 121(16):10187–10217, October 2020. doi: 10.1021/acs.chemrev.0c00665. URL <https://doi.org/10.1021/acs.chemrev.0c00665>.
- Moon, S., Zhung, W., Yang, S., Lim, J., and Kim, W. Y. PIGNet: a physics-informed deep learning model toward generalized drug–target interaction predictions. *Chemical Science*, 13(13):3661–3673, 2022. doi: 10.1039/d1sc06946b. URL <https://doi.org/10.1039/d1sc06946b>.
- Palazzesi, F., Hermann, M. R., Grundl, M. A., Pautsch, A., Seeliger, D., Tautermann, C. S., and Weber, A. BIreactive: A machine-learning model to estimate covalent warhead reactivity. *Journal of Chemical Information and Modeling*, 60(6):2915–2923, April 2020. doi: 10.1021/acs.jcim.9b01058. URL <https://doi.org/10.1021/acs.jcim.9b01058>.
- Park, S., Han, H., Kim, H., and Choi, S. Machine learning applications for chemical reactions. *Chemistry – An Asian Journal*, 17(14), May 2022. doi: 10.1002/asia.202200203. URL <https://doi.org/10.1002/asia.202200203>.
- Pattanaik, L., Ingraham, J. B., Grambow, C. A., and Green, W. H. Generating transition states of isomerization reactions with deep learning. *Physical Chemistry Chemical Physics*, 22(41):23618–23626, 2020. doi: 10.1039/d0cp04670a. URL <https://doi.org/10.1039/d0cp04670a>.
- Ramakrishnan, R., Dral, P. O., Rupp, M., and von Lilienfeld, O. A. Quantum chemistry structures and properties of 134 kilo molecules. *Scientific Data*, 1(1), August 2014. doi: 10.1038/sdata.2014.22. URL <https://doi.org/10.1038/sdata.2014.22>.
- Riniker, S. and Landrum, G. A. Better informed distance geometry: Using what we know to improve conformation generation. *Journal of Chemical Information and Modeling*, 55(12):2562–2574, November 2015. doi: 10.1021/acs.jcim.5b00654. URL <https://doi.org/10.1021/acs.jcim.5b00654>.
- Sanchez-Gonzalez, A., Godwin, J., Pfaff, T., Ying, R., Leskovec, J., and Battaglia, P. Learning to simulate complex physics with graph networks. In *International conference on machine learning*, pp. 8459–8468. PMLR, 2020.
- Sato, R., Yamada, M., and Kashima, H. Random features strengthen graph neural networks. In *Proceedings of the 2021 SIAM International Conference on Data Mining (SDM)*, pp. 333–341. SIAM, 2021.
- Satorras, V. G., Hoogeboom, E., and Welling, M. E(n) equivariant graph neural networks. In Meila, M. and Zhang, T. (eds.), *Proceedings of the 38th International Conference on Machine Learning Research*, volume 139 of *Proceedings of Machine Learning Research*, pp. 9323–9332. PMLR, 18–24 Jul 2021. URL <https://proceedings.mlr.press/v139/satorras21a.html>.
- Schütt, K., Unke, O., and Gastegger, M. Equivariant message passing for the prediction of tensorial properties and molecular spectra. In Meila, M. and Zhang, T. (eds.),

- Proceedings of the 38th International Conference on Machine Learning*, volume 139 of *Proceedings of Machine Learning Research*, pp. 9377–9388. PMLR, 18–24 Jul 2021. URL <https://proceedings.mlr.press/v139/schutt21a.html>.
- Schütt, K. T., Kessel, P., Gastegger, M., Nicoli, K. A., Tkatchenko, A., and Müller, K.-R. SchNetPack: A deep learning toolbox for atomistic systems. *Journal of Chemical Theory and Computation*, 15(1):448–455, November 2018a. doi: 10.1021/acs.jctc.8b00908. URL <https://doi.org/10.1021/acs.jctc.8b00908>.
- Schütt, K. T., Sauceda, H. E., Kindermans, P.-J., Tkatchenko, A., and Müller, K.-R. SchNet – a deep learning architecture for molecules and materials. *The Journal of Chemical Physics*, 148(24):241722, June 2018b. doi: 10.1063/1.5019779. URL <https://doi.org/10.1063/1.5019779>.
- Schütt, K. T., Gastegger, M., Tkatchenko, A., Müller, K.-R., and Maurer, R. J. Unifying machine learning and quantum chemistry with a deep neural network for molecular wavefunctions. *Nature Communications*, 10(1), November 2019. doi: 10.1038/s41467-019-12875-2. URL <https://doi.org/10.1038/s41467-019-12875-2>.
- Shi, C., Luo, S., Xu, M., and Tang, J. Learning gradient fields for molecular conformation generation. In Meila, M. and Zhang, T. (eds.), *Proceedings of the 38th International Conference on Machine Learning*, volume 139 of *Proceedings of Machine Learning Research*, pp. 9558–9568. PMLR, 18–24 Jul 2021. URL <https://proceedings.mlr.press/v139/shi21b.html>.
- Spiekermann, K., Pattanaik, L., and Green, W. H. High accuracy barrier heights, enthalpies, and rate coefficients for chemical reactions. *Scientific Data*, 9(1), July 2022a. doi: 10.1038/s41597-022-01529-6. URL <https://doi.org/10.1038/s41597-022-01529-6>.
- Spiekermann, K. A., Pattanaik, L., and Green, W. H. Fast predictions of reaction barrier heights: Toward coupled-cluster accuracy. *The Journal of Physical Chemistry A*, 126(25):3976–3986, June 2022b. doi: 10.1021/acs.jpca.2c02614. URL <https://doi.org/10.1021/acs.jpca.2c02614>.
- Stärk, H., Beaini, D., Corso, G., Tossou, P., Dallago, C., Günnemann, S., and Liò, P. 3d infomax improves gns for molecular property prediction. 2021. doi: 10.48550/ARXIV.2110.04126. URL <https://arxiv.org/abs/2110.04126>.
- Vincent, P., Larochelle, H., Bengio, Y., and Manzagol, P.-A. Extracting and composing robust features with denoising autoencoders. In *Proceedings of the 25th international conference on Machine learning*, pp. 1096–1103, 2008.
- Vincent, P., Larochelle, H., Lajoie, I., Bengio, Y., and Manzagol, P.-A. Stacked denoising autoencoders: Learning useful representations in a deep network with a local denoising criterion. *Journal of Machine Learning Research*, 11(110):3371–3408, 2010. URL <http://jmlr.org/papers/v11/vincent10a.html>.
- Wang, L., Liu, Y., Lin, Y., Liu, H., and Ji, S. Comenet: Towards complete and efficient message passing for 3d molecular graphs. *arXiv preprint arXiv:2206.08515*, 2022.
- Xie, Y., Wang, Z., and Ji, S. Noise2same: Optimizing a self-supervised bound for image denoising. *Advances in Neural Information Processing Systems*, 33:20320–20330, 2020.
- Xie, Y., Xu, Z., and Ji, S. Self-supervised representation learning via latent graph prediction. In *International Conference on Machine Learning*, pp. 24460–24477. PMLR, 2022.
- Xiong, Z., Wang, D., Liu, X., Zhong, F., Wan, X., Li, X., Li, Z., Luo, X., Chen, K., Jiang, H., and Zheng, M. Pushing the boundaries of molecular representation for drug discovery with the graph attention mechanism. *Journal of Medicinal Chemistry*, 63(16):8749–8760, August 2019. doi: 10.1021/acs.jmedchem.9b00959. URL <https://doi.org/10.1021/acs.jmedchem.9b00959>.
- Xu, M., Yu, L., Song, Y., Shi, C., Ermon, S., and Tang, J. Geodiff: A geometric diffusion model for molecular conformation generation. *arXiv preprint arXiv:2203.02923*, 2022.
- Xu, Z., Luo, Y., Zhang, X., Xu, X., Xie, Y., Liu, M., Dickerson, K., Deng, C., Nakata, M., and Ji, S. Molecule3d: A benchmark for predicting 3d geometries from molecular graphs, 2021. URL <https://arxiv.org/abs/2110.01717>.
- Yang, K., Swanson, K., Jin, W., Coley, C., Eiden, P., Gao, H., Guzman-Perez, A., Hopper, T., Kelley, B., Mathea, M., Palmer, A., Settels, V., Jaakkola, T., Jensen, K., and Barzilay, R. Analyzing learned molecular representations for property prediction. *Journal of Chemical Information and Modeling*, 59(8):3370–3388, July 2019. doi: 10.1021/acs.jcim.9b00237. URL <https://doi.org/10.1021/acs.jcim.9b00237>.
- Zaidi, S., Schaarschmidt, M., Martens, J., Kim, H., Teh, Y. W., Sanchez-Gonzalez, A., Battaglia, P., Pascanu, R.,

and Godwin, J. Pre-training via denoising for molecular property prediction. *arXiv preprint arXiv:2206.00133*, 2022.

Zhou, J., Cui, G., Hu, S., Zhang, Z., Yang, C., Liu, Z., Wang, L., Li, C., and Sun, M. Graph neural networks: A review of methods and applications. *AI Open*, 1:57–81, 2020. doi: 10.1016/j.aiopen.2021.01.001. URL <https://doi.org/10.1016/j.aiopen.2021.01.001>.

Zhou, Y., Arpit, D., Nwogu, I., and Govindaraju, V. Is joint training better for deep auto-encoders?, 2014. URL <https://arxiv.org/abs/1405.1380>.

A. Further explanations

A.1. Can easy-to-obtain geometry be interpreted as corrupted geometry?

In this work, we considered the easy-to-obtain geometry \tilde{X} as corrupted version of the correct geometry X . The following two conditions will be satisfied if \tilde{X} is actually the corrupted one:

- Regardless of the types of properties, the baseline will always have a higher MAE than the ground truth.
- The interpolated geometry of \tilde{X} and X is a less corrupted geometry than \tilde{X} . Thus, MAEs of the model using the interpolated geometry are placed between those of the baseline and the ground truth.

We have confirmed this empirically from the experiments in Tables 7 and 8. These results demonstrate that the interpolated geometry is a better input geometry than \tilde{X} for various quantum chemical properties.

Table 7: MAEs for QM9’s properties with different inputs using the EGNN. $(\tilde{X}+X)/2$, the interpolated geometry, was generated from the mean of the distance matrices of \tilde{X} and X .

| TARGET | UNIT | \tilde{X} | $(\tilde{X}+X)/2$ | X |
|----------|-------------------|-------------|-------------------|--------|
| U_0 | meV | 17.4 | 14.2 | 12.9 |
| μ | D | 0.133 | 0.0807 | 0.0350 |
| α | Bohr ³ | 0.125 | 0.0947 | 0.0759 |
| HOMO | meV | 38.4 | 33.4 | 31.2 |
| LUMO | meV | 34.4 | 28.9 | 26.6 |
| GAP | meV | 58.0 | 53.0 | 51.1 |
| R^2 | Bohr ² | 5.60 | 2.92 | 0.130 |
| C_v | cal/mol · K | 0.0445 | 0.0377 | 0.0336 |
| ZPVE | meV | 1.97 | 1.74 | 1.59 |

Table 8: MAEs (kcal/mol) of predicted barrier heights with different inputs using the 3D DimeReaction. $(\tilde{X}+X)/2$, the pairwise interpolated geometry, was generated from the mean of the pairwise distance matrices of (X^R, X^P) and (X^R, X^{TS}) .

| DATASET | \tilde{X} | $(\tilde{X}+X)/2$ | X |
|-------------|-------------|-------------------|------|
| CCST(D)-UNI | 6.49 | 5.30 | 2.38 |
| B97-D3 | 8.24 | 3.91 | 1.92 |

A.2. Gradual denoising process

In our methodology, we proceed with the denoising process for all GNN layers. Thus, denoising power may vary depending on the number of layers. The relationship between the number of GNN layers and the D-MAE of the atomic positions at the last layer was investigated using the EGNN model (see Figure 2). We note that each EGNN was trained using only the denoising loss to confirm the denoising power alone.

In particular, the denosing procoess with the small number of GNN layers could not restore X . We note that the D-MAE between the MMFF and the DFT geometries is 0.0712 Å. In this respect, we expected that if the denoising process couldn’t restore X , the corresponding denoising loss can have a negative effect on learning by maintaining a large amount compared to other losses in the training process. Therefore, based on Equation (12), we suggested a gradual denoising loss, the slightly modified version of the denoising loss, as follows:

$$\mathcal{L}_d^l = \frac{1}{n} \sum_{i=1}^n \|\mathbf{d}_{i,\text{target}}^l - \tilde{\mathbf{d}}_i^l\|_1, \quad (13)$$

$$\mathbf{d}_{\text{target}}^l = \frac{1}{L} (l\mathbf{d} + (L-l)\tilde{\mathbf{d}}), \quad (14)$$

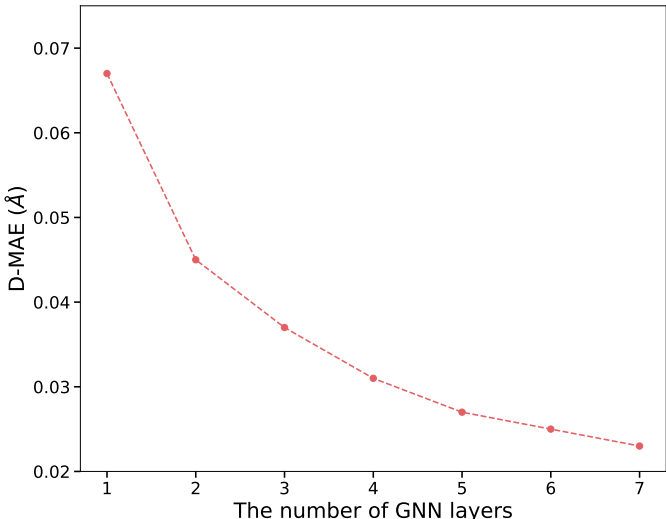


Figure 2: D-MAE according to the number of GNN layers of the EGNN. The D-MAE is measured using X and the denoised \tilde{X} derived from the last layer.

where L is the number of GNN layers, \mathbf{d} and $\tilde{\mathbf{d}}$ are distance matrices of X and \tilde{X} , respectively. We expected that the gradual denoising loss could have a positive effect on the actual target property prediction based on the fact that the interpolated geometry is also a better input geometry than \tilde{X} . Table 9 shows that gradual denoising process is useful to increase model performance. Thus, we adopted a gradual denoising loss to predict quantum chemical properties.

Table 9: Impact of each denoising task in terms of MAE. We tested gradual denoising (“OURS”), “w/o gradual denoising”, and “denoising last only” for four properties. When gradual denoising was not used, the objective of all denoising processes of GNN layers is restoring X . The “denoising last only” means that use only the denoising loss of the last GNN layer without the losses of other GNN layers.

| PROPERTY | UNIT | OURS | W/O GRADUAL DENOISING | DENOISING LAST ONLY |
|----------|-------------------|--------|-----------------------|---------------------|
| U_0 | meV | 14.5 | 15.4 | 14.9 |
| R^2 | Bohr ² | 4.08 | 4.22 | 4.97 |
| C_v | cal/mol · K | 0.0407 | 0.0413 | 0.0423 |
| μ | D | 0.0997 | 0.100 | 0.132 |

A.3. Model performance based on DFT geometry for QM9’s properties

The aim of this study is to accurately predict quantum chemical properties from easy-to-obtain geometries. Therefore, for comparison, we identified the performance of QM9’s properties prediction from X for the various models used in this work (see Table 10). For this purpose, each model was trained using only X . The same training, validation, and test datasets as in Section 4.1 were used to train and evaluate each model.

Table 10: MAEs for QM9’s properties prediction based on the DFT geometry. The results of the Transformer-M are the reported values by Luo et al. (2022).

| TARGET | UNIT | EGNN | SCHNET | DIMENET++ | TRANSFORMER-M |
|----------|-------------------|--------|--------|-----------|---------------|
| U_0 | meV | 12.9 | 16.96 | 8.99 | 14.78 |
| μ | D | 0.035 | 0.0391 | 0.0382 | - |
| α | Bohr ³ | 0.071 | 0.0859 | 0.0583 | - |
| HOMO | meV | 31.2 | 44.3 | 25.5 | 26.5 |
| LUMO | meV | 26.6 | 34.9 | 20.8 | 23.8 |
| GAP | meV | 51.1 | 68.6 | 43.0 | - |
| R^2 | Bohr ² | 0.130 | 0.170 | 0.342 | - |
| C_v | cal/mol · K | 0.0336 | 0.0313 | 0.0255 | - |
| ZPVE | meV | 1.59 | 1.67 | 1.30 | - |

A.4. Understanding different denoising effects depending on properties for OOD data

In general, the prediction error for out-of-distribution (OOD) data can be larger than that of in-distribution data. The results of Pearson correlation coefficients between D-MAE and P-MAE in Table 3 could be attributed to generalization, thereby requiring further analyses. Thus, we identified whether the increase is due to the generalization issue. To this purpose, we use a scaffold split to measure denoising effects for the molecules in OOD. The split is based on the Bemis–Murcko scaffold (Bemis & Murcko, 1996) implemented in RDKit (Contributors, 2021) library. Table 11 shows that on average, the more accurate prediction is possible as \tilde{X} approaches X as in Table 3. Both results imply our proposed “denoising from the perspective of geometry” worked effectively regardless of the generalization issue.

 Table 11: The Pearson correlation coefficients between D-MAE and P-MAE (ρ_{DP}) for R^2 , μ , and U_0 in the QM9_M. We verified the coefficients for molecules out-of-distributions. The coefficient values were compared for the baseline and the model using our method.

| PROPERTY | EGNN _{BASE} | EGNN _{OURS} |
|----------|----------------------|----------------------|
| R^2 | 0.484 | 0.667 |
| μ | 0.469 | 0.601 |
| U_0 | 0.195 | 0.216 |

B. Loss derivation

Our training objective is to maximize MI, and we derive a lower bound from Proposition 3.3. Because MI is intractable, the practical target is to maximize the lower bounds of the three conditional entropies, $-H(X|\tilde{X})$, $-H(Y|\tilde{X})$, and $-H(Y|X)$.

Our method employs a similar objective to that of DAE, which aims to learn a compressed representation M of a corrupted input \tilde{X} by maximizing the MI between them. To ensure that the training process of DAE is consistent with theoretically derived objective $-H(X|\tilde{X})$, we first verify that DAE training target maximize $-H(X|\tilde{X})$. Proposition B.1 confirms that training DAE can maximize $I(X; \tilde{X})$ when the encoder is injective and deterministic.

Proposition B.1. *Let the joint distribution $q(X, \tilde{X}, M)$ be parameterized by θ of the encoder parameter and $p(X, \tilde{X}, M)$ be parameterized by θ and θ' of the decoder parameter. If the encoder f_θ is deterministic and injective, conditional cross-entropy of $X|M$ is equivalent to that of $X|\tilde{X}$*

$$-\mathbb{E}_{q(X, \tilde{X})} [\log p(X|\tilde{X})] = -\mathbb{E}_{q(X, M)} [\log p(X|M)].$$

Proof.

$$\begin{aligned}
 \mathbb{E}_{q(X,M)}[\log p(X|M)] &= \int \int q(X, M) \log p(X|M) dM dX && \text{(DAE training target)} \\
 &= \int \int \int q(X, \tilde{X}, M) \log p(X|M) dM dX d\tilde{X} \\
 &= \int \int \int q(X, \tilde{X}) q(M|X, \tilde{X}) \log p(X|M) dM dX d\tilde{X} \\
 &= \int \int q(X, \tilde{X}) \int q(M|\tilde{X}) \log p(X|M) dM dX d\tilde{X} && (M \text{ is solely dependent on } \tilde{X}) \\
 &= \int \int q(X, \tilde{X}) \log p(X|M = f_\theta(\tilde{X})) dX d\tilde{X} && (M|\tilde{X} \sim \delta_{f_\theta(X)}(M)) \\
 &= \int \int q(X, \tilde{X}) \log p(X|\tilde{X}) dX d\tilde{X} && (f_\theta \text{ is injective)} \\
 &= \mathbb{E}_{q(X,\tilde{X})}[\log p(X|\tilde{X})]
 \end{aligned}$$

□

Our method employs a sequential denoising process, which can be interpreted as multiple encoder-decoder structures being stacked. In this scenario, the denoised output from the previous layer is fed back into the next layer. Notably, even in this case, maximizing MI between \tilde{X} and the intermediate representation Z eventually maximize MI between \tilde{X} and X , which can be proved in a similar way as we did for Proposition B.1.

Proposition B.2. *Let Z be a random variable of intermediate representation of \tilde{X} and $q(\tilde{X}, Z, X)$ be a joint distribution. If Z is determined by \tilde{X} with injective function f , for any joint distribution $p(\tilde{X}, Z, X) = q(\tilde{X}, Z)p(X|Z)$ the two conditional cross-entropy is equal*

$$-\mathbb{E}_{q(X,\tilde{X})}[\log p(X|\tilde{X})] = -\mathbb{E}_{q(X,Z)}[\log p(X|Z)].$$

Proof.

$$\begin{aligned}
 \mathbb{E}_{q(X,Z)}[\log p(X|Z)] &= \int \int q(X, Z) \log p(X|Z) dZ dX \\
 &= \int \int \int q(X, \tilde{X}, Z) \log p(X|Z) dZ dX d\tilde{X} \\
 &= \int \int \int q(X, \tilde{X}) q(Z|X, \tilde{X}) \log p(X|Z) dZ dX d\tilde{X} \\
 &= \int \int q(X, \tilde{X}) \int q(Z|\tilde{X}) \log p(X|Z) dZ dX d\tilde{X} && (Z \text{ is solely dependent on } \tilde{X}) \\
 &= \int \int q(X, \tilde{X}) \log p(X|Z = f(\tilde{X})) dX d\tilde{X} && (Z|\tilde{X} \sim \delta_{f(X)}(Z)) \\
 &= \int \int q(X, \tilde{X}) \log p(X|\tilde{X}) dX d\tilde{X} && (f \text{ is injective)} \\
 &= \mathbb{E}_{q(X,\tilde{X})}[\log p(X|\tilde{X})]
 \end{aligned}$$

□

Proposition B.2 shows that with a stacked architecture of L encoder-decoder layers, maximizing mutual information between the corrupted input \tilde{X} and input X can still be achieved by maximizing the conditional cross-entropy between the intermediate representation $Z = F_{L-1} \circ F_{L-2} \circ \dots \circ F_1(X)$ and X , where F_i means encoder-decoder of i^{th} layer. This conditional cross-entropy is equivalent to the conditional cross-entropy between X and the representation M_z that is the last encoder's output, as established in Proposition B.1, which can be practically evaluated as a general DAE denoising loss. Therefore, the tractable lower bound is obtained as $\mathbb{E}_{q_{\mathcal{D}}(X)q_{\mathcal{D}}(\tilde{X}|X)}[f_{\text{loss}}(X, g_L \circ f_L(Z = F_{L-1} \circ F_{L-2} \circ \dots \circ F_1(\tilde{X})))]$

according to the loss function f_{loss} , where $q_{\mathcal{D}}$ is empirical distribution and f_L and g_L means the encoder and decoder, respectively.

Let (x, \tilde{x}, y) be a sampled data point from the training dataset \mathcal{D} . The positions of x and \tilde{x} are p and \tilde{p} , respectively. We practically denoised only positional information in the denoising process. This is a natural choice given that x and \tilde{x} have the same atom composition. Meanwhile, it is impossible to directly use the position p and \tilde{p} in Euclidean space. Under our problem setting, the property y is invariant to the SE(3) group action on the corresponding geometry. This means that Cartesian coordinates p and \tilde{p} cannot be unique geometric representations of x and \tilde{x} . Since our encoders and decoders should be deterministic to meet assumption, the geometric representations need to be represented as an unique representation that is invariant to the SE(3) transformation. We used atom pair distance as a unique geometric representation, which is a method adopted in many molecular generative models recently (Shi et al., 2021; Xu et al., 2022). Since distance space is a metric space with naturally defined metric, l_p , we can create an appropriate probability measure. In this work, we assume that the distributions in distance space and in Euclidean space would be expressed locally as the same family, and the l_1 loss was used in practice. For pairwise distance mapping $D : p \in \mathbb{R}^{N \times 3} \rightarrow \mathbf{d} \in \mathbb{R}^{N \times N}$ and the last decoder output $\tilde{\mathbf{d}}^L = D(g_L \circ f_L \circ F_{L-1} \circ \dots \circ F_1(\tilde{x}))$, denoising loss is as Equation (15),

$$\mathcal{L}_{\mathbf{d}} = \sum_{(x_i, \tilde{x}_i, y_i) \in \mathcal{D}} [l_1(\mathbf{d}_i, \tilde{\mathbf{d}}_i^L)], \quad (15)$$

where i imply index of sampled data from \mathcal{D} . Based on Propositions B.1 and B.2, it is feasible to calculate the loss not only in the final layer of the decoder but also in all layers. As a result, Equation (16) can be used to express the loss in this scenario.

$$\mathcal{L}_{\mathbf{d}} = \sum_{l=1}^L \mathcal{L}_{\mathbf{d}}^l = \sum_{l=1}^L \sum_{(x_i, \tilde{x}_i, y_i) \in \mathcal{D}} [l_1(\mathbf{d}_i, \tilde{\mathbf{d}}_i^l)] \quad (16)$$

Here, $\tilde{\mathbf{d}}_i^l$ is from l^{th} decoder output.

$I(X; Y)$ and $I(\tilde{X}; Y)$ can be maximized as general property prediction model does by maximizing the lower bound $\mathbb{E}_{q(Y, \tilde{X})} [\log p(Y | \tilde{X})]$. For the property prediction layer h , the property prediction loss is described at Equation (17), where $\hat{y}_{\text{corrupted}} = h \circ f_L \circ F_{L-1} \circ \dots \circ F_1(\tilde{x})$ and $\hat{y}_{\text{correct}} = h \circ f_L \circ f_{L-1} \circ \dots \circ f_1(x)$. In practice, we used l_1 loss function. Without loss of generality, according to Propositions B.1 and B.2, the lower bound can be interpreted as an lower bound of MI between last encoder output M_z and Y . Therefore, in the training process, the MI between representation M_z and Y is also maximized.

$$\begin{aligned} \mathcal{L}_{y, \text{corrupted}} &= \sum_{(x_i, \tilde{x}_i, y_i) \in \mathcal{D}} [l_1(y_i, \hat{y}_{i, \text{corrupted}})] \\ \mathcal{L}_{y, \text{correct}} &= \sum_{(x_i, \tilde{x}_i, y_i) \in \mathcal{D}} [l_1(y_i, \hat{y}_{i, \text{correct}})] \end{aligned} \quad (17)$$

C. Proof of propositions

C.1. Conditionally independent random variables

Proof of Proposition 3.2. From the definition of conditional mutual information, we start from below.

$$\begin{aligned} I(\tilde{X}; Y | X) &= H(\tilde{X} | X) + H(Y | X) - H(\tilde{X}, Y | X) \\ &= \mathbb{E}_{p(\tilde{X}, X, Y)} \left[-\log \frac{p(\tilde{X} | X)p(Y | X)}{p(\tilde{X}, Y | X)} \right] \\ &= \mathbb{E}_{p(\tilde{X}, X, Y)} \left[-\log \frac{p(\tilde{X}, X)p(Y, X)/p(X)^2}{p(\tilde{X}, Y, X)/p(X)} \right] \\ &= \mathbb{E}_{p(\tilde{X}, X, Y)} \left[-\log \frac{p(\tilde{X}, X)p(Y, X)}{p(\tilde{X}, Y, X)p(X)} \right] \end{aligned}$$

$$\begin{aligned}
 &= \mathbb{E}_{p(\tilde{X}, X, Y)} \left[-\log \frac{p(Y, X)/p(X)}{p(\tilde{X}, Y, X)/p(\tilde{X}, X)} \right] \\
 &= \mathbb{E}_{p(\tilde{X}, X, Y)} \left[-\log \frac{p(Y|X)}{p(Y|\tilde{X}, X)} \right] \\
 &= \mathbb{E}_{p(\tilde{X}, X, Y)} \left[-\log \frac{p(Y|X)}{p(Y|\tilde{X}, X)} \right] \quad (\text{conditional independence}) \\
 &= 0
 \end{aligned}$$

While MLE target objective is maximization of $-H(Y|\tilde{X})$ which is same as below.

$$\begin{aligned}
 -H(Y|\tilde{X}) &= [H(Y) - H(Y|\tilde{X})] \\
 &= I(\tilde{X}; X; Y) + \cancel{I(\tilde{X}; Y|X)} \\
 &= I(\tilde{X}; X; Y)
 \end{aligned}$$

□

C.2. MLE objective is same as MI given Assumption 3.1

Proof of Proposition 3.3. We need to proof the followings first.

$$H(X) - I(\tilde{X}; X) \geq I(X; Y) - I(\tilde{X}; X; Y) \quad \forall \text{ random variables } \tilde{X}, X, Y$$

$$\begin{aligned}
 \text{LHS} &= H(X|\tilde{X}) \\
 \text{RHS} &= I(X; Y) - [I(X; Y) - I(X; Y|\tilde{X})] \\
 &= I(X; Y|\tilde{X}) \\
 &= \mathbb{E}_{p(\tilde{X}, X, Y)} \left[-\log \frac{p(X|\tilde{X})p(Y|\tilde{X})}{p(X, Y|\tilde{X})} \right] \\
 &= \mathbb{E}_{p(\tilde{X}, X, Y)} \left[-\log \frac{p(X|\tilde{X})}{p(X|\tilde{X}, Y)} \right] \\
 &= H(X|\tilde{X}) - H(X|\tilde{X}, Y)
 \end{aligned}$$

Because conditional entropy is non-negative, LHS \geq RHS.

By applying above statements, we can derive the two inequality.

$$\begin{aligned}
 I(\tilde{X}; X; Y) &\geq I(\tilde{X}; X) + I(X; Y) - H(X) \\
 &= -[H(X) - I(\tilde{X}; X)] - [H(Y) - I(X; Y)] + H(Y) \\
 &= -H(X|\tilde{X}) - H(Y|X) + H(Y)
 \end{aligned}$$

$$\begin{aligned}
 I(\tilde{X}; X; Y) &\geq I(\tilde{X}; Y) + I(X; Y) - H(Y) \\
 &= -[H(Y) - I(\tilde{X}; Y)] - [H(Y) - I(X; Y)] + H(Y) \\
 &= -H(Y|\tilde{X}) - H(Y|X) + H(Y)
 \end{aligned}$$

Adding two inequality, we are done.

□

D. Experimental Details

D.1. Parameter Details

QM9_M. We used the reported hyperparameters optimized for QM9 from previous studies for EGNN (Satorras et al., 2021), SchNet (Schütt et al., 2018a), DimeNet++ (Gasteiger et al., 2020a), and Transformer-M (Luo et al., 2022). Additionally, to

Table 12: The search space of λ for training OURS for QM9

| TARGET | EGNN | DIMENET++ | SCHNET |
|----------|-----------------------|-----------|---------------------------|
| U_0 | [0.1, 0.5, 1.0, 10.0] | 0.1 | [0.1 0.5, 1.0, 5.0, 10.0] |
| μ | [0.1, 0.5, 1.0, 10.0] | 0.1 | [0.1 0.5, 1.0, 5.0, 10.0] |
| α | 0.1 | 0.1 | [0.1 0.5, 1.0, 5.0, 10.0] |
| HOMO | 0.1 | 0.1 | 0.1 |
| LUMO | 0.1 | 0.1 | 0.1 |
| GAP | 0.1 | 0.1 | 0.1 |
| R^2 | [0.1, 0.5, 1.0, 10.0] | 0.1 | [0.1 0.5, 1.0, 5.0, 10.0] |
| C_v | 0.1 | 0.1 | 0.1 |
| ZPVE | 0.1 | 0.1 | 0.1 |

train Transformer-M, The mode distribution (p_{2D} , p_{3D} , $p_{2D\&3D}$) is set to (0.25,0.5,0.25) reported as the best performance for properties of QM9. The search space of λ is specified in Table 12.

Reaction Barrier Prediction. We used the same hyperparameters as Spiekermann et al. (2022a). In the case of 3D DimeReaction and OURS, we used different epochs and batch sizes from the official repository (Table 5). Note that we did not use additional input. The search space of λ is specified in Table 14.

Table 13: The hyperparameters for training 3D DimeReaction

| PARAMETER | CCSD(T)-UNI | B97-D3 |
|----------------|-------------|--------|
| EPOCH | 200 | 200 |
| BATCH SIZE | 32 | 64 |
| WARM-UP EPOCHS | 3 | 3 |

 Table 14: The search space of λ for CCSD(T)-UNI and B97-D3 datasets

| PARAMETER | CCSD(T)-UNI | B97-D3 |
|-----------|-----------------------------|-----------------------------|
| λ | [0.005,0.01,0.05,0.1,0.5,1] | [0.005,0.01,0.05,0.1,0.5,1] |

E. Message Passing Scheme for DimeNet++

Since DimeNet++ (Gasteiger et al., 2020a), which incorporates additional angle information during the training process, has a different message-passing scheme than SchNet (Schütt et al., 2018a) and EGNN (Satorras et al., 2021), we introduce the corresponding message-passing and positional update scheme as follows:

$$a_{ji}^l = f_{\text{RBF}}(D(p^{l-1})_{ji}) \quad (18)$$

$$a_{kj,ji}^l = f_{\text{SBF}}(D(p^{l-1})_{ji}, A(p^{l-1})_{kj,ji}) \quad (19)$$

$$m_{ji}^1 = \sigma([h_j^0 || h_i^0 || a_{ji}^1]W + b) \quad (20)$$

$$m_{ji,2-hop}^{(l+1)} = \sum_{k \in N_j \setminus i} f_{\text{int}}(m_{kj}^l, a_{ji}^l, a_{kj,ji}^l) \quad (21)$$

$$m_{ji}^{(l+1)} = f_{\text{update}}(m_{ji}^l, m_{ji,2-hop}^{(l+1)}) \quad (22)$$

$$p_i^{l+1} = p_i^l + \sum_{j \in N(i)} (p_i^l - p_j^l) \theta_{\text{pos}}(m_{ji}^{(l+1)}; \theta^l) \quad (23)$$

The Equations (18) to (22) are referred from DimeNet (Gasteiger et al., 2020b) and DimeNet++ (Gasteiger et al., 2020a). f_{RBF} , f_{SBF} , and $A : p \in \mathbb{R}^{N \times 3} \rightarrow \alpha \in \mathbb{R}^{N \times N}$ are the radial basis function (RBF), the 2D spherical Fourier-Bessel function (SBF), and the mapping A from position space to angle space, respectively. The crucial aspect of the above equations is that our method updates the geometry in each layer, leading to modifications in both the radial basis and the spherical Fourier-Bessel representations. This contrasts with the vanilla DimeNet++, where Equations (18) and (19) demonstrate that RBF and SBF remain static.